Contents lists available at: http://qu.edu.iq

Al-Qadisiyah Journal for Engineering Sciences

Journal homepage: https://qjes.qu.edu.iq

Research Paper

Thermo-magnetohydrodynamic natural convection in corrugated enclosures with a clear nanofluid layer and a porous layer saturated by Al_2O_3/Ethylene glycol nanofluid

Nowras Saad Abdown and Isam Mejbel Abed

Mechanical Engineering Department, University of Babylon, Hillah, Babylon 51001, Iraq.

ARTICLE INFO

Article history:
Received 00 mmm yyyy
Received in revised form 00 mmmmm YYYY
Accepted 00 mmmm yyyy

keyword:
Natural convection
Corrugated enclosure
Nanofluid
Porous medium
MHD

ABSTRACT

Natural convection heat transfer in corrugated enclosures has attracted increasing attention due to its importance in thermal management applications. However, the combined effects of wall corrugation, porous media, ethylene glycol–based nanofluids, and magnetic field control have not been sufficiently addressed. In the present study, a numerical investigation is carried out to analyze thermo-magnetohydrodynamic natural convection inside a corrugated enclosure subjected to different heating configurations. The enclosure is divided into two regions: an upper region filled with an ethylene glycol–based nanofluid and a lower porous layer saturated with the same nanofluid. Three heating cases are considered, namely an externally heated corrugated cylinder, an upper heated wall, and an externally heated circular boundary. The governing equations are solved using the finite element method under steady-state conditions. The effects of Rayleigh number ($10^4 \rightarrow 10^6$), Hartmann number ($0 \rightarrow 60$), Darcy number ($10^{-5} \rightarrow 10^{-3}$), and magnetic field inclination angle ($0° \rightarrow 135°$) are examined at a fixed nanoparticle volume fraction of 0.02. The results show that increasing the Rayleigh number enhances heat transfer, while the magnetic field intensity suppresses convection. Among all cases, the externally heated corrugated cylinder provides the highest thermal performance, and the ethylene glycol–based nanofluid enhances the average Nusselt number by up to 48% at $Ra = 10^6$.

1. Introduction

Natural convection is driven by buoyancy forces induced from a density difference in the fluid as a result of temperature. This passive heat transfer process is of strategic importance for many engineering and energy systems, such as building thermal management, electronic cooling, solar energy systems, nuclear reactor safety, and thermal storage applications. Khanafer et al. [1] reported that in both cases, flow circulations (and Nusselt numbers) are strongly modulated by nanoparticle concentration and enclosure shape. The development of nanofluids, i.e., nanoparticle-dispersed fluids, has brought an advancement to convective heat transfer through heat exchangers. It is reported that Brownian diffusion and thermophoresis of nanoparticles can greatly affect the heat transfer enhancement profile, temperature distribution, and flow field in a nanofluid-filled cavity by Buongiorno and Hu [2]. Wang and Mujumdar [3] reviewed these developments and highlighted challenges related to nanoparticle dispersion, stability, and effective property modeling. Nield and Kuznetsov [4] revealed that porosity resistance and the concentration of nanoparticles influenced thermal performance. Sheikhzadeh [5], previous studies have examined nanoparticle transport effects on natural convection of Al_2O_3–water nanofluids in square cavities, considering Brownian motion and thermophoresis. Transport models generally showed better agreement with experiments and indicated a negligible influence of the Dufour effect. Both homogeneous and transport models reported reduced heat transfer with increasing nanoparticle concentration, while transport models predicted a decrease with increasing particle size. Chamkha and Rashad [6] illustrated that, in general an existence of an internal heat source would have a significant effect on the flow and temperature field distribution, particularly if its position and the properties of the nanofluid used were taken into account. Rashad et al. [7] and Miroshnichenko et al. [8] also highlighted the impact of Hartmann number and orientation of the magnetic field for the magnetohydrodynamic (MHD) case.

There has been recent work on complex geometries and coupled physical phenomena. Abdulkadhim et al. [9] investigated improved MHD convection of a wavy porous enclosure by highlighting the role of the wall shapes and magnetic field directions. Zidan et al. [10] concluded that Rayleigh, Darcy, and Hartmann numbers are found to together control entropy generation and heat transfer. More detailed computations in 2025–2026 with a realistic configuration and state-of-the-art numerical methods helped to raise the field. Zhang [11] found that both the attitude of the enclosure and internal eccentricity have significant influences on vortex formation and local heat transfer. Hasan et al. [12] used data-supplemented simulations for corrugated boxes and obtained better estimates of heat transfer. El-Sheikh et al. [13] studied entropy generation in nanofluid saturated porous cavities with inclined magnetic fields. Abdulkadhim et al. [8], Rahimi and Chamkha [14], on compound solutions have established that corrugation, and magnetic field orientation in combination with porous media charge to improve heat transfer as well as reduce entropy generation. However, works involving corrugated porous enclosures, alumina/ethylene glycol nanofluids, and inclined magnetic fields are scarce. The compiled influence of Rayleigh number, Hartmann number, Darcy number, and magnetic field orientation with nanoparticle volume fraction has not been addressed to date.

*Corresponding Author.
E-mail address: eng.isam.m@uobabylon.edu.iq ; Tel: (+964) 780-151 8934 (Isma Mejbel)

https://doi.org/10.30772/qjes.000.000.000

Nomenclature

A	Amplitude of wavy wall	Kr	Thermal conductivity ratio
$A1$	Porous resistance parameter	Ks	Thermal conductivity of solid particles
C	Buoyancy correction parameter	Kss	Solid matrix thermal conductivity
$C1$	Thermal diffusivity ratio	m,n	Auxiliary model parameters
$C3$	Viscous–thermal parameter	muf	Dynamic viscosity of base fluid
$C4$	Effective thermal diffusivity ratio	$munf$	Dynamic viscosity of nanofluid
$C5$	Porous viscosity factor	N	Number of wall undulations
Cp	Specific heat of base fluid	Nu	Nusselt number
$Cpnf$	Effective heat capacity of nanofluid	o	Porosity function
Cps	Specific heat of solid particles	Pr	Prandtl number
Da	Darcy number	Ra	Rayleigh number
F	Dimensionless buoyancy force parameter	$rhof$	Density of base fluid
Ha	Hartmann number	$rhonf$	Density of nanofluid
K	Thermal conductivity of base fluid	$rhos$	Density of solid particles
$Keff$	Effective thermal conductivity in porous medium	Tc	Dimensionless cold wall temperature
Knf	Thermal conductivity of nanofluid	vf	Kinematic viscosity of base fluid

Khan et al. [15], studied the problem of buoyancy-driven magnetized flow for Al_2O_3/water–ethylene glycol (50:50) nanofluid through an octagonal enclosure with heated circular blocks computationally. The equations are non-dimensionalized, and the bilayer equations are discretized via a Galerkin finite element exchange scheme. It was further observed that the heat transfer augmentation increases with increasing particle volume fraction and Reynolds number. The findings indicate the excellent promise of nanofluids for advanced thermal applications involving engineering equipment and energy systems. Ghasemi et al. [16] studied the MHD natural convection of a water–Al_2O_3 nanofluid in an enclosure having isothermal vertical walls and adiabatic horizontal walls. It is found that Ra enhances heat transfer while Ha reduces it. The influence of nanoparticle volume fraction is found to be dependent on the combined effect of Rayleigh and Hartmann numbers. Samrat Hansda et al. [17], investigated Free convection in a U-shaped enclosure is an important area of research because it plays critical roles in electronic cooling, energy application, and solar thermal storage. It is found that the heat transfer is significantly affected by the Rayleigh number, aspect ratio, baffle arrangement, nanoparticle volume fraction, and nanofluids always give rise to a superior thermal performance. Numerical methods, such as the finite volume method and the lattice Boltzmann method, have been extensively used to study the deep flow complexity. To go a step further, the multimodule optimization under multi-physics conditions, including porous media, magnetic fields, and entropy optimization, must be investigated. The present work fills this gap by performing an analytical study of MHD natural convection in a corrugated porous enclosure saturated with Al_2O_3/ethylene glycol nanofluid. A systematic investigation is carried out regarding the influences of major governing parameters on flow and heat transfer behaviors. By combining corrugated geometry, porous media, nanofluid-based formulation, and inclined magnetic field effects into a unified base, the study presents new findings in relation to passive heat transfer intensification processes for energy-saving thermal control.

2. Geometrical description and mathematical formulation

The present study considers a two-dimensional enclosure with corrugated upper and lower walls. The enclosure is divided horizontally into two layers. The upper layer is occupied by an ethylene-glycol-based nanofluid, while the lower layer consists of the same nanofluid saturating a porous medium. This configuration is selected to represent a realistic thermal system in which clear fluid and porous regions coexist. The left and right vertical walls of the enclosure are assumed to be thermally insulated. The remaining boundaries are subjected to different thermal conditions depending on the heating configuration under consideration. The corrugated shape of the enclosure walls is introduced to disturb the thermal boundary layer and promote fluid mixing inside the cavity. Fluid flow in the clear nanofluid region is governed by the incompressible Navier–Stokes equations, whereas the flow inside the porous layer is described using the Darcy–Brinkman model. Heat transfer in both regions is modeled using the energy equation under the assumption of local thermal equilibrium between the fluid and the porous matrix. The influence of an externally applied inclined magnetic field is also considered to investigate magnetohydrodynamic effects on the flow and thermal behavior. The computational domain and boundary conditions are illustrated schematically in Fig. 1. For clarity, the dimensions of the computational domain corresponding to the physical configuration shown in Fig. 2 are specified as follows:
The computational domain extends from $x = -0.2$ to $x = 1.3$ in the horizontal direction, while the interface between the upper and lower layers is located within the vertical range $0.3 \leq y \leq 0.7$. Three distinct heating configurations are investigated in this study. In the first configuration, the external corrugated cylinder is maintained at a hot temperature, while the remaining boundaries are kept cold, and the vertical side walls are considered adiabatic (thermally insulated).

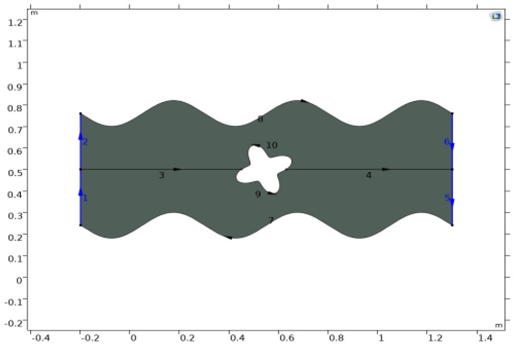

Figure 1. Geometric model and dimensions of the corrugated enclosure.

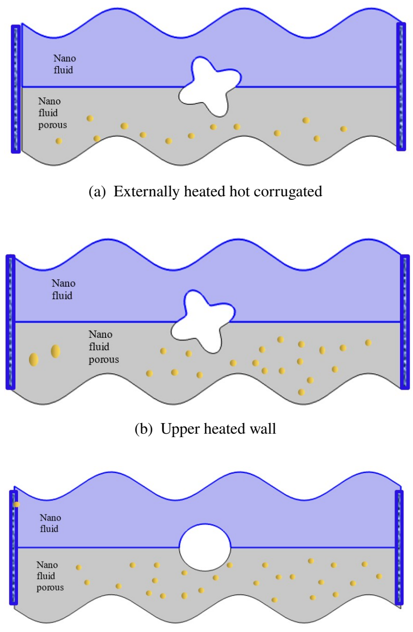

(a) Externally heated hot corrugated

(b) Upper heated wall

(c) Externally heated hot circular

Figure 2. Physical model with different heating configurations.

In the second configuration, the upper wall of the enclosure is heated, whereas the other walls and internal elements are maintained at a cold temperature, and the side walls remain thermally insulated. In the third configuration, the external circular boundary is heated, while all other boundaries are kept cold, with adiabatic conditions applied to the left and right walls. The influence of the inclined magnetic field on the thermal behavior of the enclosure is examined at four inclination angles, namely 0°, 45°, 90°, and 135°. In addition, the geometry of the corrugated internal cylinder is represented using parametric equations adopted from Tayebi et al. [18], as presented in Eq. 1 and 2.

$$x = [R + A\ sin(2\pi NS)] \times cos(2\pi S) \tag{1}$$

$$y = [R + A\ sin(2\pi NS)] \times sin(2\pi S) \tag{2}$$

Here, A is 0.02, and the outer radius R is 0.1 with four undulations. The parameter S ranges from a minimum of 0 to a maximum of 1. Left and right side walls are described by the Eq. 3 and 4.

$$x = A \times (1 - cos(2N\pi S)) \tag{3}$$

$$y = S \tag{4}$$

The amplitude of the corrugated upper and lower walls is 0.06, which has two ripples on each wall. Here, A is the wall waviness amplitude ($A = 0.06$), and N refers to the number of undulations ($N = 2$). This corrugated configuration is introduced to disturb the thermal boundary layer and enhance fluid mixing within the enclosure. Several assumptions are adopted in the present analysis. The working nanofluid is considered incompressible, Newtonian, and the flow is assumed to be laminar. The effects of internal heat generation and thermal radiation are neglected. All thermophysical properties of the nanofluid are assumed to be constant, except for the density variation, which is taken into account through the Boussinesq approximation. In addition, local thermal equilibrium between the porous medium and the nanofluid is assumed.

3. Physical model description

In the present numerical study, the governing equations describing fluid flow and heat transfer inside the enclosure are presented. The working fluid is modeled as an incompressible nanofluid, and the flow is assumed to be two-dimensional, steady, and laminar. In regions where the porous medium exists, the Brinkman model extended Darcy model, is employed to account for both viscous and inertial resistance effects. The buoyancy force induced by temperature differences is modeled using the Boussinesq approximation, in which density variations are considered only in the body force term. Based on these considerations, the conservation equations of mass, momentum, and energy are formulated in dimensional form for both the clear fluid and porous regions as follows [18–21].

Continuity Equation

The mass conservation equation ensures incompressibility, Eq. 5.

$$\frac{\partial u}{\partial x} + \frac{\partial v}{\partial y} = 0 \tag{5}$$

Momentum Equations:

The momentum equation for natural convection, incorporating the Boussinesq approximation for density variation, is given by:

X-Momentum Equation, Eq. 6

$$\rho_{nf}\left(u\frac{\partial u}{\partial x} + v\frac{\partial v}{\partial y}\right) = -C_1\frac{\partial p}{\partial x} + C_2\mu_{nf}\left(\frac{\partial^2 u}{\partial x^2} + \frac{\partial^2 v}{\partial y^2}\right) - \\ -C_3\mu_{nf}\frac{u}{K} + C_1 B_o^2\sigma_{nf}\left[V sin(\gamma)\ cos(\gamma) - U\ sin^2(\gamma)\right] \tag{6}$$

Y-momentum Equation, Eq. 7

$$\rho_{nf}\left(u\frac{\partial u}{\partial x} + v\frac{\partial v}{\partial y}\right) = -C_1\frac{\partial p}{\partial x} + C_2\mu_{nf}\left(\frac{\partial^2 u}{\partial x^2} + \frac{\partial^2 v}{\partial y^2}\right) - \\ -C_3\mu_{nf}\frac{u}{K} + C_1\rho_{nf}\beta_{nf}g(T - T_c) + \\ + C_1 B_o^2\sigma nf\left[U sin(\gamma)\ cos(\gamma) - V\ cos^2(\gamma)\right] \tag{7}$$

Energy Equation

The energy equation governing heat transfer in the nanofluid is given by, Eq. 8.

$$u\frac{\partial u}{\partial x} + v\frac{\partial v}{\partial y} = C_4\left(\frac{\partial^2 T}{\partial x^2} + \frac{\partial^2 T}{\partial y^2}\right) \tag{8}$$

After rearranging, the non-dimensional governing equations are as Eq. 9.

$$\left.\begin{array}{lcr} X = \dfrac{x}{H} & ; & Y = \dfrac{y}{H} \\ A = \dfrac{L}{H} & ; & U = \dfrac{uH}{\alpha_{bf}} \\ V = \dfrac{vH}{\alpha_{bf}} & ; & \theta = \dfrac{T - T_c}{T_h - T_c} \\ P = \dfrac{pH^2}{\rho_{na}\alpha_{bf}^2} & ; & Pr = \dfrac{\nu_{bf}}{\alpha_{bf}} \\ Ra = \dfrac{g\beta_{bf}(T_h - T_c)H^3}{\alpha_{bf}\nu_{bf}} & ; & Da = \dfrac{K}{H^2} \\ k_r = \dfrac{k_w}{k_{na}} & ; & Ha = B_o H\sqrt{\sigma_{bf}\rho_{na}\nu_{na}} \end{array}\right\} \tag{9}$$

The dual-layer configuration for non-dimensional forms is provided below: **Mass Conservation Expression**, Eq. 10

$$\frac{\partial u}{\partial x} + \frac{\partial v}{\partial y} = 0 \tag{10}$$

X-momentum Equation, Eq. 11:

$$U\frac{\partial U}{\partial X} + V\frac{\partial V}{\partial Y} = -C_1\frac{\partial P}{\partial X} + C_2\frac{\mu_{nf}}{\rho_{nf}\alpha_f}\left(\frac{\partial^2 U}{\partial X^2} + \frac{\partial^2 U}{\partial Y^2}\right) - \\ -C_3\frac{\mu_{nf}}{\rho_{nf}\alpha_f}\frac{U}{Da} + C_1 PrHa^2\left[V sin(\gamma) - U\ sin^2(\gamma)\right] \tag{11}$$

Governing Equation for the Vertical Momentum (Y-direction), Eq. 12

$$U\frac{\partial V}{\partial X} + V\frac{\partial V}{\partial Y} = -C_1\frac{\partial P}{\partial Y} + C_2\frac{\mu_{nf}}{\rho_{nf}\alpha_f}\left(\frac{\partial^2 V}{\partial X^2} + \frac{\partial^2 V}{\partial Y^2}\right) - \\ -C_3\frac{\mu_{nf}}{\rho_{nf}\alpha_f}\frac{V}{Da} + C_1\frac{(\rho\beta)_{nf}}{\rho_f\beta_{nf}}Ra\theta + \\ + C_1 Ha^2 Pr\left[U sin(\gamma)\ cos(\gamma) - V cos^2(\gamma)\right] \tag{12}$$

Energy Equation, Eq. 13

$$U\frac{\partial \theta}{\partial X} + V\frac{\partial \theta}{\partial Y} = C_4\left(\frac{\partial^2 \theta}{\partial X^2} + \frac{\partial^2 \theta}{\partial Y^2}\right) \tag{13}$$

The following expressions define the effective thermophysical properties of the nanofluid used in this study Eq. 14, 15, 16 and 17, [18, 20, 22, 23].

$$\alpha_{na} = \frac{k_{nf}}{(\rho C_p)_{nf}} \tag{14}$$

$$\rho_{na} = (1 - \phi)\rho_f + \phi\rho_p \tag{15}$$

$$(\rho c_p)_{nf} = (1 - \phi)(\rho c_p)_f + \phi(\rho c_p)_p \tag{16}$$

$$(\rho\beta)_{na} = (1 - \phi)(\rho\beta)_f + \phi(\rho\beta)_{sp} \tag{17}$$

The constants utilized in Eqs. 11, 12 and 13 are provided in Table 1 for the corresponding layers; [20],and Physical and thermophysical properties of ethylene glycol and Al_2O_3 nanoparticles in Table 2, [18].

Table 1. Coefficient Constant of Nanofluid and Nano-Porous layers [24].

Layer	C_1	C_2	C_3	C_4
Nanofluid Layer	1	1	0	α_{nf}/α_f
Nano – Porous Layer	ε^2	ε	ε^2	α_{eff}/α_f

Table 2. Physical and thermophysical properties of ethylene glycol and Al_2O_3 nanoparticles [18].

Properties	$Cp(kg/m^3)$	$Cp(J/(kg\ K))$	$K(W/(m\ K))$	$\beta(1/K)$
$C_2H_3O_2$	1114	2140	0.252	2.5×10^{-5}
Al_2O_3	3970	765	40	0.85×10^{-5}

3.1 Boundary conditions

Appropriate thermal and velocity boundary conditions were imposed to accurately represent the physical model, Eq. 18. A no-slip condition was applied on all solid boundaries, such that the velocity components satisfy $U = V = 0$. Three different heating configurations were considered as follows:

- Case (1): The external surface of the internal corrugated circular cylinder was maintained at a constant hot temperature ($\theta = 1$). The upper and lower walls of the enclosure were kept at a cold temperature ($\theta = 0$), while the left and right vertical walls were thermally insulated, expressed as $\frac{\partial\theta}{\partial x} = 0$.
- Case (2): The upper wall of the enclosure was heated ($\theta = 1$), whereas the lower wall and the external surface of the internal cylinder were maintained at a cold temperature ($\theta = 0$). The left and right vertical walls remained thermally insulated ($\frac{\partial\theta}{\partial x} = 0$).
- Case (3): The external surface of the internal circular heat source was heated ($\theta = 1$), while the upper and lower walls were kept cold ($\theta = 0$). The left and right walls were considered adiabatic ($\frac{\partial\theta}{\partial x} = 0$).

$$\left.\begin{aligned}
&\theta_{po} = \theta_{na} \\
&\frac{\partial\theta_{na}}{\partial X} = \frac{K_{eff}\partial\theta_{po}}{K_{na}\partial X} \\
&\Psi_{po} = \Psi_{na} \\
&\frac{\partial\Psi_{na}}{\partial X} = \frac{\partial\Psi_{po}}{\partial X} \\
&\Omega_{po} = \Omega_{na} \\
&\frac{\partial\Omega_{na}}{\partial X} = \frac{\partial\Omega_{po}}{\partial X} \\
&\mu_{po}\left(\frac{\partial U_{po}}{\partial Y} + \frac{\partial V_{po}}{\partial X}\right) = \mu_{na}\left(\frac{\partial U_{na}}{\partial Y} + \frac{\partial V_{na}}{\partial X}\right) \\
&P_{po} = P_{na} \\
&\frac{\partial P_{po}}{\partial X} = \frac{\partial P_{na}}{\partial Y}
\end{aligned}\right\} \tag{18}$$

The local and average Nusselt numbers were evaluated along the heated boundary for each case, Eq. 19 and 20. The average value was obtained by integrating the local distribution over the heated surface and then taking the mean to assess the overall heat-transfer performance [23].

$$Nu_{loc} = \frac{\partial\theta}{\partial n} \tag{19}$$

$$Nu_{avg} = \frac{1}{2\pi}\left[\frac{k_{na}}{k_{bf}}\right]\int_{o}^{\pi} Nu_{loc}(\varphi)d\varphi + \frac{1}{2\pi}\left[\frac{k_{eff}}{k_{bf}}\right]\int_{\pi}^{2\pi} Nu_{loc}(\varphi)d\varphi \tag{20}$$

3.2 Numerical simulation approach and validation procedure

The simulation was carried out by numerically solving the governing equations under steady-state conditions using a finite element scheme. To guarantee numerical precision, the mesh quality was repeatedly verified, and a convergence tolerance of 10^{-5} was adopted, as represented in the Eq. 21 [9]:

$$\frac{\Sigma|\zeta_{i,j}^{n+1} - \zeta_{i,j}^{n}|}{|\zeta_{i,j}^{n+1}|} \le 10^{-5} \tag{21}$$

3.3 Mesh generation and dependency

The numerical simulations were carried out using COMSOL Multiphysics based on the finite element method (FEM). A mesh independence test was performed to ensure the accuracy and reliability of the numerical results. The average Nusselt number was employed as the convergence indicator. Several mesh levels, ranging from extremely coarse to extremely fine, were examined. The outcomes of the grid sensitivity analysis are summarized in Table 3 and 4. Based on this analysis, the extremely fine mesh was selected for all subsequent simulations. The numerical solution was considered converged when the residuals dropped below 10^{-5} as shown in Fig. 3 and 4.

Table 3. Grid sensitivity analysis of the Nusselt number for the corrugated cylinder.

Grid size	Number of Elements	Nu	Error (%)
Extremely coarse	1250	23.1200	——
Extra coarse	1750	23.6800	2.3649
Coarser	2900	24.1800	2.0670
Coarse	4450	24.5600	1.5472
Normal	6200	24.7900	0.9278
Fine	8900	24.9200	0.5217
Finer	13500	24.9900	0.2801
Extra fine	21820	25.0300	0.1598
Extremely fine	33400	25.0400	0.0399

Table 4. Grid sensitivity analysis of the Nusselt number for the circular heated body.

Grid size	Number of Elements	Nu	Error (%)
Extremely coarse	1100	18.0600	——
Extra coarse	1600	18.5200	2.4838
Coarser	2650	18.9200	2.1142
Coarse	4050	19.2400	1.6632
Normal	5750	19.4500	1.0797
Fine	8250	19.5600	0.5624
Finer	12700	19.6200	0.3058
Extra fine	20900	19.6500	0.1527
Extremely fine	30200	19.6600	0.0509

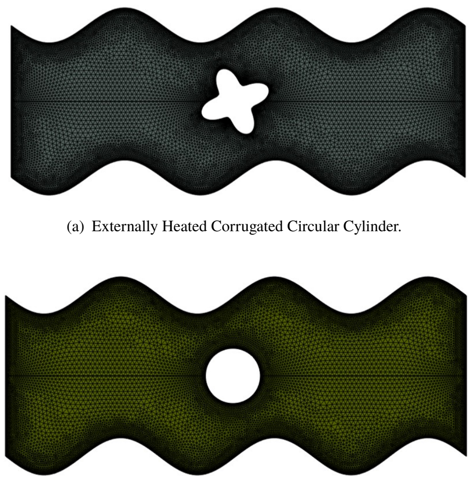

(a) Externally Heated Corrugated Circular Cylinder.

(b) Externally Heated Circular Heat Source.

Figure 3. Finite element mesh distributions for externally heated geometries.

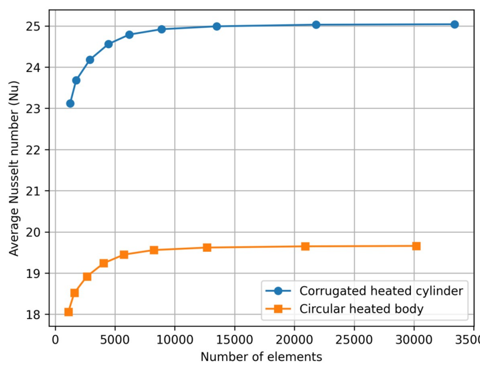

Figure 4. Effect of mesh density on the average Nusselt number for the corrugated cylinder and circular heated body.

3.4 Numerical validation of the present model

The present numerical model was validated by comparing the obtained stream function contours and the corresponding maximum values (ψ_{max}) with those reported by Nehad Abid Allah et al. [20], as illustrated in Fig. 5, under identical conditions of $Ra = 10^6$ and $Ha = 60$. A strong agreement is observed in the flow structure, vortex distribution, and overall circulation behavior, indicating that the stream function intensity decreases with decreasing Darcy number. The relative deviation between the present results and the reference study remains within 0.1%–3.7%, which confirms the accuracy, robustness, and reliability of the proposed numerical approach. To assess the reliability and consistency of the present numerical model, as shown in Fig. 6, a validation study was conducted through comparison with the streamline results reported by Ali Al-Zamily [21]. Both investigations examined natural convection within a square enclosure at $Ra = 10^7$ and $Da = 10^{-5}$, while considering different nanoparticle volume fractions ($\phi = 0$, 0.05, and 0.1) and a heated wall length ratio of $L_{pm} = L/3$. The obtained streamline contours exhibit excellent agreement with those presented by Al-Zamily in terms of flow structure, vortex formation, and symmetry characteristics. This strong correspondence verifies the accuracy of the numerical formulation and confirms the robustness of the adopted computational approach.

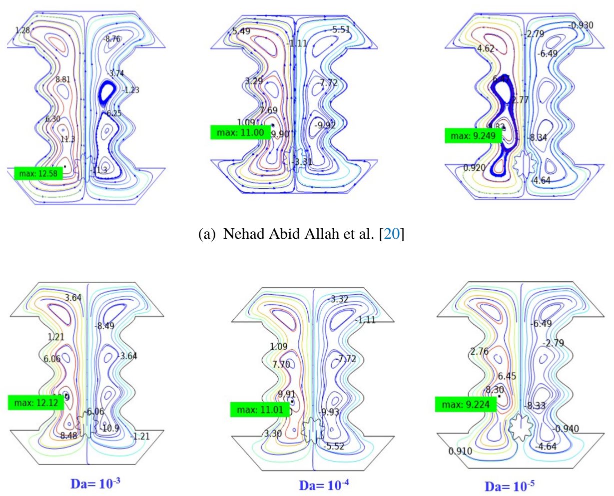

(a) Nehad Abid Allah et al. [20]

(b) Present Study.

Figure 5. Comparison of Stream Function Contours Between the Present Study and Nehad et al. [20] at $Ra = 10^6$ and $Ha = 60$.

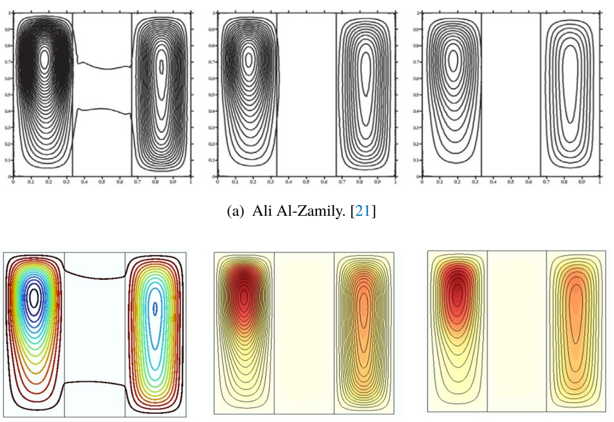

(a) Ali Al-Zamily. [21]

(b) Present Simulation.

Figure 6. Validation of the Present Numerical Model Using Streamline Comparison.

4. Results and discussion

The numerical outcomes of the present investigation. The study systematically examines the influence of the primary controlling parameters on both heat transfer and fluid flow characteristics. They comprised the Rayleigh number (Ra), which represents buoyancy-induced convection; the Hartmann number (Ha), reflecting the effect of the imposed magnetic field on the fluid motion; and the Darcy number (Da), which describes the influence of the porous medium's permeability on flow resistance.

4.1 Stream function analysis under different Rayleigh numbers

Figure 7 illustrates the stream function contours for the three heating configurations at different Rayleigh numbers ($Ra = 10^4$, 10^5, and 10^6), while keeping $Ha = 40$, $Da = 10^{-3}$, $\gamma = 45$, and $\phi = 0.02$ constant. At $Ra = 10^4$, the flow inside the enclosure is very weak for all cases, indicating a conduction-dominated heat transfer regime. The maximum stream function values remain low due to weak buoyancy forces. Specifically, the highest value of the stream function is observed in Case 1 (externally heated corrugated cylinder) with $\psi_{max} = 0.94199$, followed by Case 2 (upper heated wall) with $\psi_{max} = 0.86322$, and Case 3 (externally heated circular source) with $\psi_{max} = 0.85610$. These small values confirm limited fluid circulation and weak natural convection at low Rayleigh numbers. When the Rayleigh number increases to $Ra = 10^5$, buoyancy forces become more pronounced, leading to a clear enhancement in flow circulation and the formation of larger vortical structures. The maximum stream function values increase significantly to $\psi_{max} = 9.955$ for Case 1, $\psi_{max} = 8.5262$ for Case 2, and $\psi_{max} = 8.3258$ for Case 3. This behavior indicates a transition from conduction-dominated heat transfer to a mixed convection regime. At $Ra = 10^6$, natural convection becomes fully developed and dominates the flow field. Strong and continuous circulation cells occupy most of the enclosure, particularly around the heated regions. The stream function reaches its highest values, with $\psi_{max} = 12.1863$ for Case 1, $\psi_{max} = 11.7886$ for Case 2, and $\psi_{max} = 11.3108$ for Case 3, reflecting vigorous buoyancy-driven flow and enhanced convective heat transfer. Overall, the comparison among the three heating configurations shows that Case 1 (externally heated corrugated cylinder) consistently produces the strongest flow circulation at all Rayleigh numbers, followed by Case 2 (upper heated wall) and Case 3 (externally heated circular source). This confirms that the externally heated corrugated cylinder configuration provides the most effective enhancement of natural convection and overall thermal performance.

4.2 Isothermal contours analysis at different Rayleigh numbers

Figure 8 illustrates the isothermal contours for the three heating configurations at $Ra = 10^4$, 10^5, and 10^6, while keeping $Ha = 40$, $Da = 10^{-3}$, $\gamma = 45$, and $\phi = 0.02$ constant. At $Ra = 10^4$: The isotherms are smooth, closely spaced, and nearly parallel throughout the enclosure, indicating that heat transfer is dominated by conduction due to weak buoyancy forces. The high-temperature region remains confined near the heated surfaces, and no clear thermal plumes are observed, reflecting limited fluid motion. At $Ra = 10^5$: As the Rayleigh number increases, the isothermal contours become increasingly distorted and elongated, revealing the growing influence of buoyancy forces and the onset of convective heat transfer. Thermal energy is transported farther away from the heated regions, leading to improved thermal mixing inside the enclosure. At $Ra = 10^6$: Highly non-uniform isotherms and pronounced thermal plumes appear, particularly around the heated zones. This behavior confirms that natural convection becomes the dominant heat transfer mechanism, producing stronger temperature gradients near the cold walls and enhanced heat transport throughout the cavity.

4.3 Effect of Hartmann number on flow structure (stream function analysis)

Figure 9 illustrates the stream function contours for the three heating configurations at different Hartmann numbers ($Ha = 0$, 40, and 60), while keeping $Ra = 10^6$, $Da = 10^{-3}$, $\gamma = 45$, and $\phi = 0.02$ constant. At $Ha = 0$ the absence of a magnetic field allows buoyancy-driven flow to develop freely without Lorentz force suppression. The strongest circulation is observed for the upper heated wall configuration (Case 2), where the maximum stream function reaches $\psi_{max} \approx 14.652$, due to the extended heated surface that enhances buoyancy forces. The externally heated cylinder (Case 1) follows with $\psi_{max} \approx 14.332$, as localized heating around the cylindrical surface intensifies flow circulation but over a smaller region. The weakest circulation occurs for the externally heated circular source (Case 3) with $\psi_{max} \approx 13.782$, owing to its limited thermal influence. Overall, the flow strength at Ha = 0 follows the order:
upper heated wall > externally heated cylinder > externally heated circular source, highlighting the role of heating configuration in controlling natural convection intensity.
At $Ha = 40$ When the magnetic field is applied, a noticeable suppression of fluid motion is observed for all cases. The Lorentz force generated by the interaction between the induced electric currents and the magnetic field acts

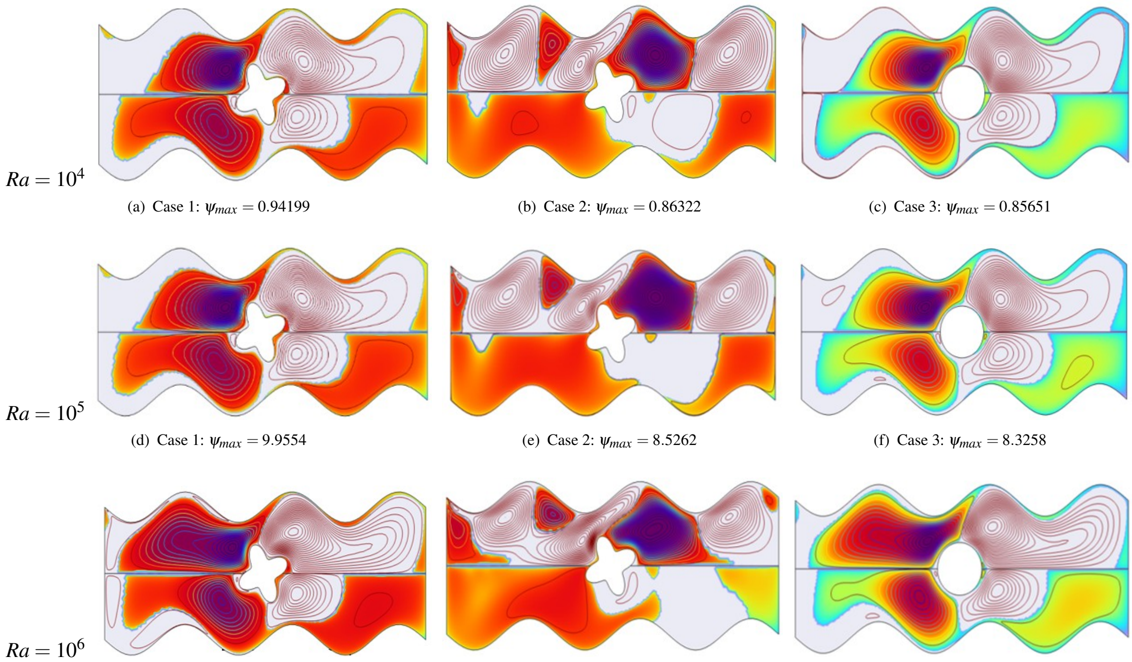

(a) Case 1: $\psi_{max} = 0.94199$ (b) Case 2: $\psi_{max} = 0.86322$ (c) Case 3: $\psi_{max} = 0.85651$

(d) Case 1: $\psi_{max} = 9.9554$ (e) Case 2: $\psi_{max} = 8.5262$ (f) Case 3: $\psi_{max} = 8.3258$

(g) Case 1: $\psi_{max} = 12.1863$ (h) Case 2: $\psi_{max} = 11.7886$ (i) Case 3: $\psi_{max} = 11.31084$

Figure 7. Stream function contours at different Rayleigh numbers ($Ra = 10^4$, 10^5, and 10^6) for the three-heating configuration, obtained at $Ha = 40$, $Da = 10^{-3}$, $\gamma = 45°$, and $\phi = 0.02$.

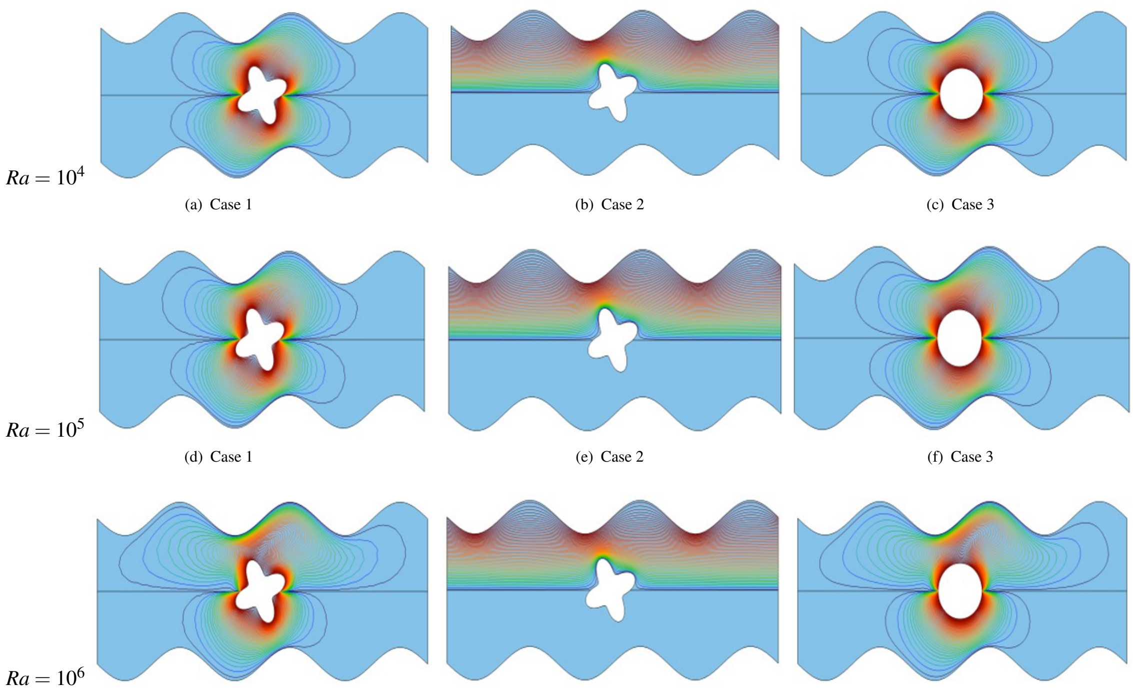

(a) Case 1 (b) Case 2 (c) Case 3

(d) Case 1 (e) Case 2 (f) Case 3

(g) Case 1 (h) Case 2 (i) Case 3

Figure 8. Isothermal contours at various Rayleigh numbers ($Ra = 10^4$, 10^5, and 10^6) for the three-heating configuration, obtained at $Ha = 40$, $Da = 10^{-3}$, $\gamma = 45°$, and $\phi = 0.02$.

as a resistive force opposing the flow. As a result, the stream function values decrease to $\psi_{max} \approx 12.1863$, 11.7886, and 11.31084 for Cases 1, 2, and 3, respectively. Although convection remains dominant, the circulation strength is clearly weakened compared to the $Ha = 0$ case. At $Ha = 60$ Further increasing the Hartmann number intensifies the magnetic damping effect. The Lorentz force significantly suppresses the velocity field, leading to weaker and more confined vortical structures. The maximum stream function values further reduce to $\psi_{max} \approx 10.589$, 10.613, and 10.531 for Cases 1, 2, and 3, respectively. At this high Hartmann number, the differences between the three heating configurations become less pronounced, indicating that the magnetic field strongly controls the flow behavior and limits buoyancy-induced circulation. Overall Observation. In general, increasing the Hartmann number from 0 to 60 leads to a substantial reduction in flow strength for all heating configurations due to magnetic damping. This confirms the dominant role of the Lorentz force

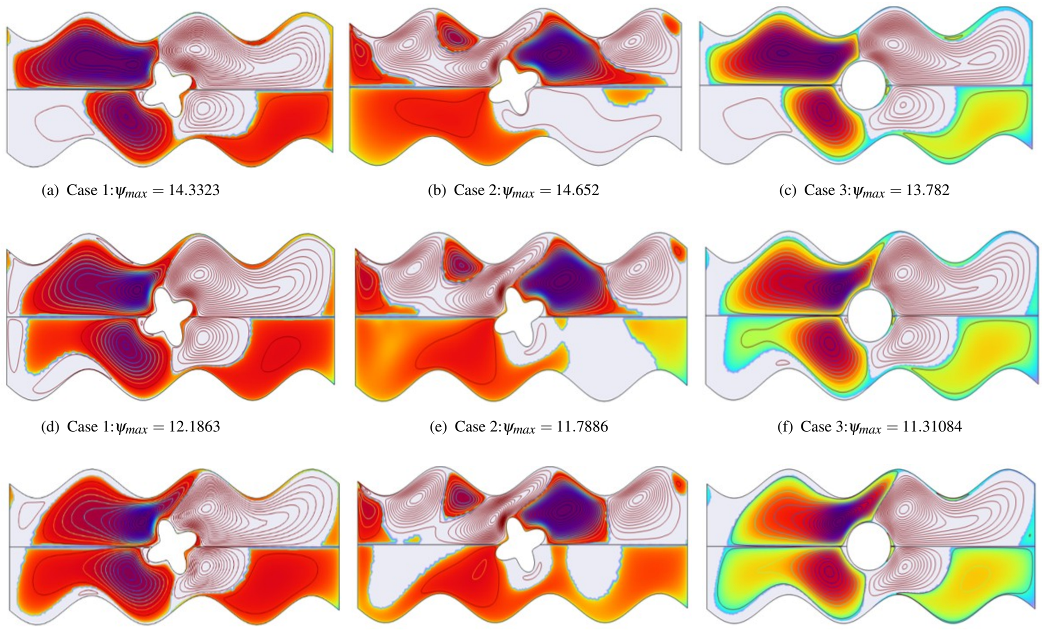

$Ha = 0$ — (a) Case 1: $\psi_{max} = 14.3323$; (b) Case 2: $\psi_{max} = 14.652$; (c) Case 3: $\psi_{max} = 13.782$

$Ha = 40$ — (d) Case 1: $\psi_{max} = 12.1863$; (e) Case 2: $\psi_{max} = 11.7886$; (f) Case 3: $\psi_{max} = 11.31084$

$Ha = 60$ — (g) Case 1: $\psi_{max} = 10.589$; (h) Case 2: $\psi_{max} = 10.6136$; (i) Case 3: $\psi_{max} = 10.5318$

Figure 9. Stream function contours at different Hartmann numbers ($Ha = 0$, 40, and 60) for the three-heating configuration, obtained at $Ra = 10^6$, $Da = 10^{-3}$, $\gamma = 45°$, and $\phi = 0.02$.

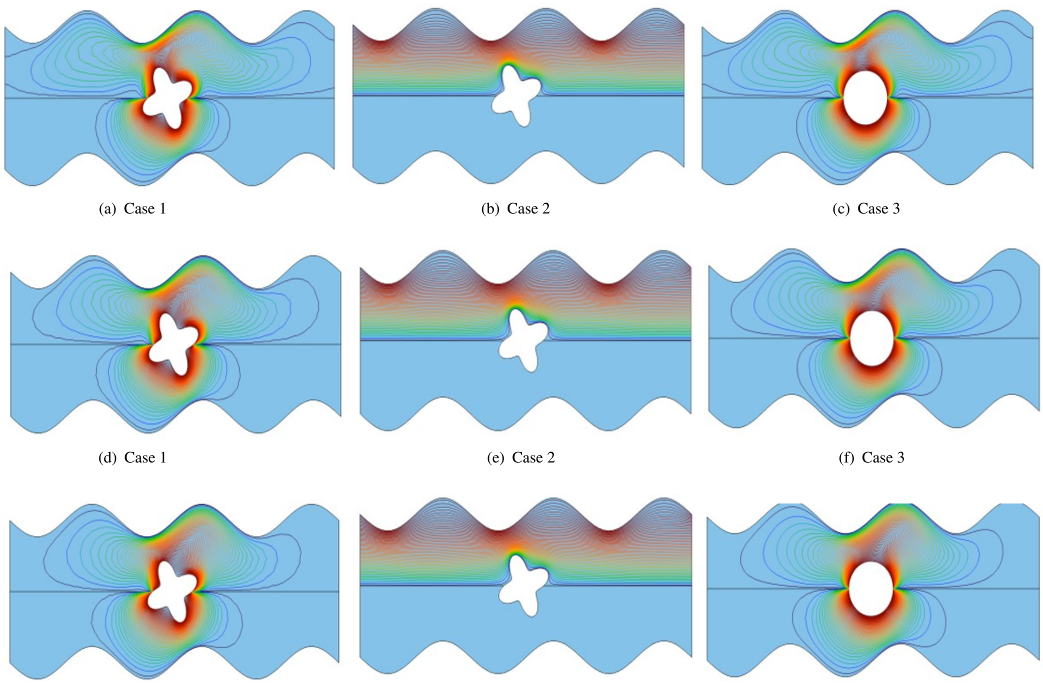

$Ha = 0$ — (a) Case 1; (b) Case 2; (c) Case 3

$Ha = 40$ — (d) Case 1; (e) Case 2; (f) Case 3

$Ha = 60$ — (g) Case 1; (h) Case 2; (i) Case 3

Figure 10. Isothermal contours at various Hartmann numbers ($Ha = 0$, 40, and 60) for the three-heating configuration, obtained at $Ra = 10^6$, $Da = 10^{-3}$, $\gamma = 45°$, and $\phi = 0.02$.

in suppressing natural convection and stabilizing the flow within the enclosure under strong magnetic field conditions. Figure 10 illustrates the isothermal contours for the three heating configurations at different Hartmann numbers ($Ha = 0$, 40, and 60) under fixed conditions of $Ra = 10^6$, $Da = 10^{-3}$, $\gamma = 45$, and $\phi = 0.02$. At $Ha = 0$, the isotherms are highly distorted, indicating strong buoyancy-driven convection and active thermal mixing inside the enclosure. As the Hartmann number increases to $Ha = 40$, the magnetic field suppresses fluid motion through the Lorentz force, resulting in smoother isotherms and reduced thermal plume intensity. When $Ha = 60$, convection is further weakened, and the isotherms become more uniform and stratified, reflecting a transition toward conduction-dominated heat transfer. Among the three configurations, the externally heated cylinder (Case 1) exhibits the most pronounced isotherm deformation at all Hartmann numbers, while the upper heated wall (Case 2) and externally heated circular source (Case 3) show relatively weaker thermal activity. Overall, increasing Ha leads to a clear reduction in convective heat transfer within the enclosure.

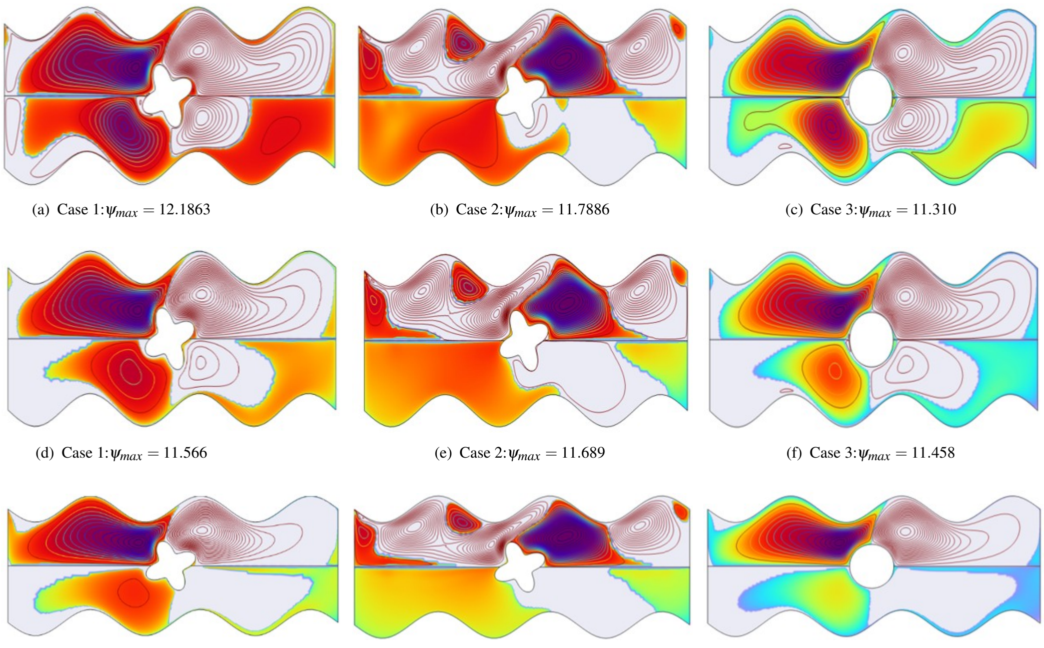

$Da = 10^{-3}$

(a) Case 1: $\psi_{max} = 12.1863$ (b) Case 2: $\psi_{max} = 11.7886$ (c) Case 3: $\psi_{max} = 11.310$

$Da = 10^{-4}$

(d) Case 1: $\psi_{max} = 11.566$ (e) Case 2: $\psi_{max} = 11.689$ (f) Case 3: $\psi_{max} = 11.458$

$Da = 10^{-5}$

(g) Case 1: $\psi_{max} = 9.856$ (h) Case 2: $\psi_{max} = 9.997$ (i) Case 3: $\psi_{max} = 8.599$

Figure 11**.** Stream function contours at different Darcy numbers ($Da = 10^{-3}$, 10^{-4}, and 10^{-5}) for the three-heating configuration, obtained at $Ra = 10^6$, $Ha = 40$, $\gamma = 45°$, and $\phi = 0.02$.

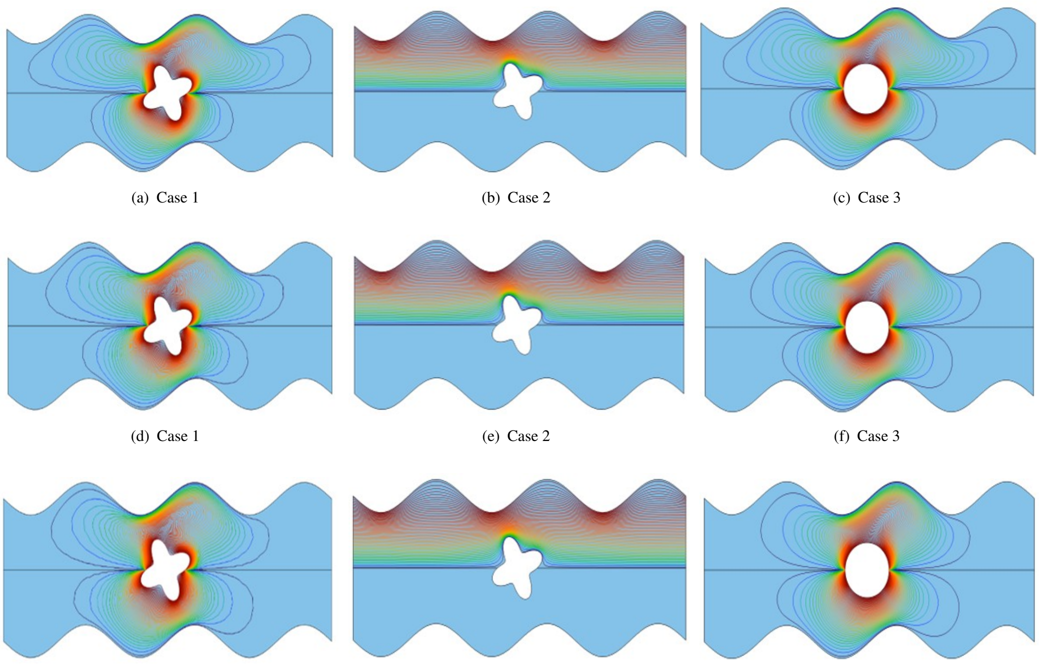

(a) Case 1 (b) Case 2 (c) Case 3

(d) Case 1 (e) Case 2 (f) Case 3

(g) Case 1 (h) Case 2 (i) Case 3

Figure 12**.** Isothermal contours at various Darcy numbers ($Da = 10^{-3}$, 10^{-4}, and 10^{-5}) for the three-heating configuration, obtained at $Ra = 10^6$, $Ha = 40$, $\gamma = 45°$, and $\phi = 0.02$.

4.4 Effect of darcy number on flow characteristics

Figure 11 illustrates the effect of the Darcy number ($Da = 10^{-3}$, 10^{-4}, and 10^{-5}) on the stream function contours for the three heating configurations at fixed conditions of $Ra = 10^6$, $Ha = 40$, $\gamma = 45$, and $\phi = 0.02$. $Da = 10^{-3}$ At $Da = 10^{-3}$, the porous medium exhibits high permeability, allowing strong buoyancy-driven fluid penetration and the formation of intense circulation cells inside the enclosure. The maximum stream function values reach: $\psi_{max} = 12.186$ for Case 1 (externally heated cylinder), $\psi_{max} = 11.788$ for Case 2 (upper heated wall), $\psi_{max} = 11.310$ for Case 3 (externally heated circular source). These relatively high values indicate vigorous natural convection and dominant fluid circulation within the porous enclosure. $Da = 10^{-4}$ When the Darcy number decreases to $Da = 10^{-4}$, the resistance of the porous medium increases, leading to a moderate reduction in flow strength. The maximum stream function values become: $\psi_{max} = 11.566$ for Case 1, $\psi_{max} = 11.685$ for Case 2, $\psi_{max} = 11.458$ for Case 3. Compared with $Da = 10^{-3}$, the stream function decreases by approximately 5.1% in Case 1 and 1.3% in Case 3, while a slight increase of about 0.9% is observed in Case 2. This behavior suggests that, at intermediate permeability, the upper heated wall configuration can

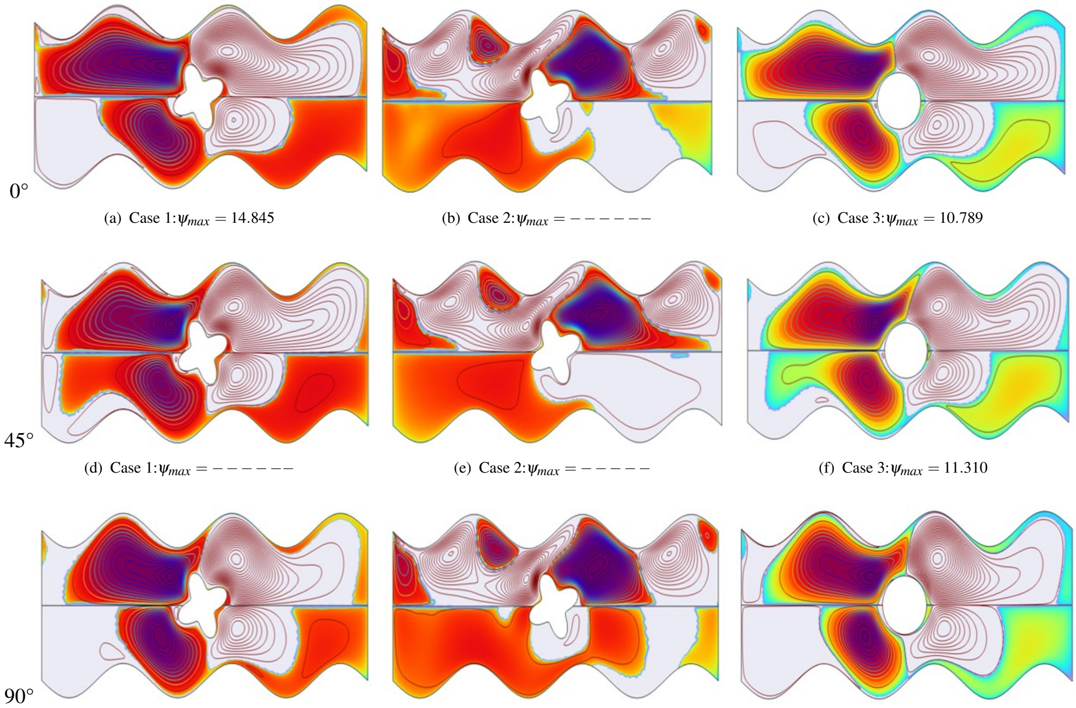

(a) Case 1: $\psi_{max} = 14.845$ (b) Case 2: $\psi_{max} = ------$ (c) Case 3: $\psi_{max} = 10.789$

(d) Case 1: $\psi_{max} = ------$ (e) Case 2: $\psi_{max} = -----$ (f) Case 3: $\psi_{max} = 11.310$

(g) Case 1: $\psi_{max} = 8.3276$ (h) Case 2: $\psi_{max} = -----$ (i) Case 3: $\psi_{max} = 7.6517$

Figure 13**.** Stream function contours at different inclination angles ($\gamma = 0°$, $45°$, and $90°$) for the three- heating configuration, obtained at $Ra = 10^6$, $Ha = 60$, $Da = 10^{-3}$, and $\phi = 0.02$.

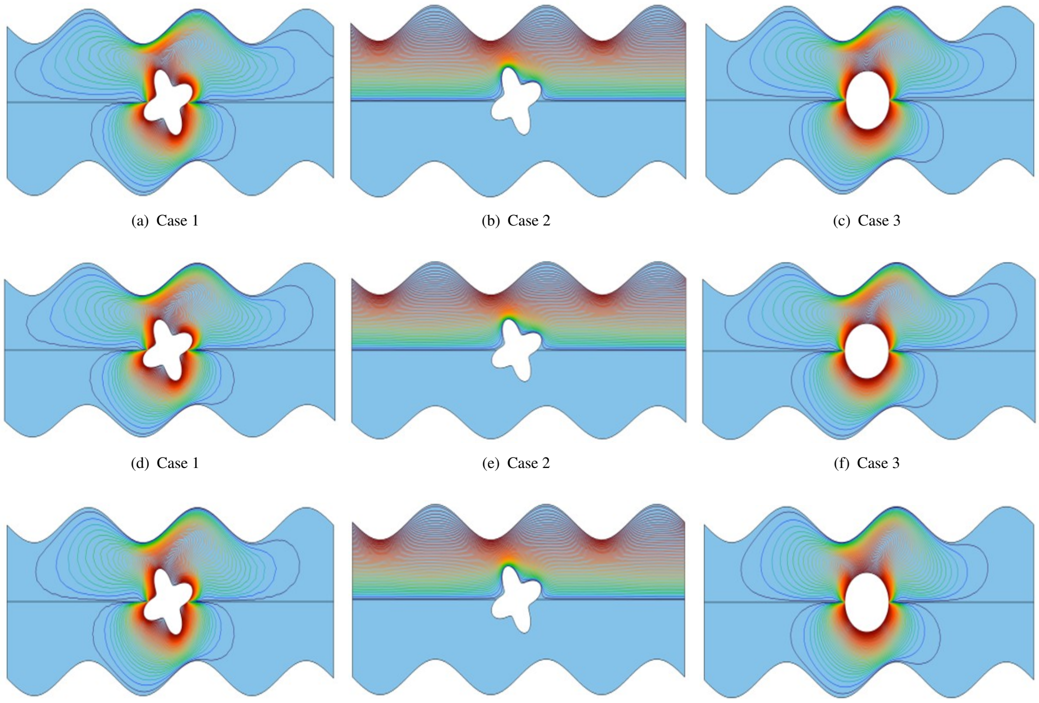

(a) Case 1 (b) Case 2 (c) Case 3

(d) Case 1 (e) Case 2 (f) Case 3

(g) Case 1 (h) Case 2 (i) Case 3

Figure 14**.** Isothermal contours at various inclination angles ($\gamma = 0°$, $45°$, and $90°$) for the three-heating configuration, obtained at $Ra = 10^6$, $Ha = 60$, $Da = 10^{-3}$, and $\phi = 0.02$.

maintain a more organized circulation structure due to favorable buoyancy distribution in the upper layer. $Da = 10^{-5}$ At $Da = 10^{-5}$, the permeability of the porous medium is significantly reduced, resulting in a strong suppression of fluid motion. The maximum stream function values further decrease to: $\psi_{max} = 9.8566$ for Case 1, $\psi_{max} = 9.9978$ for Case 2, $\psi_{max} = 8.599$ for Case 3. This corresponds to an overall reduction of approximately 19.1%, 15.2%, and 24.0% for Cases 1, 2, and 3, respectively, compared to $Da = 10^{-3}$. The flow becomes weaker and more localized near the heated regions, indicating a transition toward a conduction-dominated heat transfer regime. Overall Trend. In general, increasing the Darcy number enhances fluid circulation and strengthens natural convection by reducing porous resistance. Conversely, decreasing Da increases flow resistance, weakens vortex intensity, and suppresses convective transport. Among the three heating configurations, Case 3 is the most sensitive to porous resistance, while Cases 1 and 2 maintain relatively stronger circulation at higher permeability levels. Figure 12 illustrates the effect of the Darcy number ($Da = 10^{-3}$, 10^{-4}, and 10^{-5}) on the temperature distribution inside the enclosure for the three heating cases, while keeping $Ra = 10^6$, $Ha = 40$, $\gamma = 45$, and $\phi = 0.02$ constant. At $Da = 10^{-3}$, the porous medium exhibits high permeability, allowing strong convective motion. The isothermal contours are highly distorted and non-uniform, with pronounced thermal plumes extending from the heated regions toward the cold boundaries, indicating convection-dominated heat transfer. As the Darcy number decreases to $Da = 10^{-4}$, the resistance of the porous medium increases, leading to weaker fluid circulation. Consequently, the isotherms become smoother and less distorted, reflecting a reduced convective contribution and a gradual shift toward conduction-dominated heat transfer. At $Da = 10^{-5}$, the low permeability significantly suppresses fluid motion. The isothermal contours appear nearly parallel and concentrated around the heat sources, confirming the dominance of heat conduction and a substantial reduction in convective heat transport. Overall, the isothermal results confirm that higher Darcy numbers enhance convective heat transfer and improve thermal mixing, whereas lower Darcy numbers restrict fluid motion and promote conduction-dominated heat transfer, in good agreement with the stream function and Nusselt number analyses.

4.5 Effect of magnetic field inclination angle on stream function

Figure 13 illustrates the influence of the magnetic field inclination angle ($\gamma = 0°$, $45°$, and $90°$) on the stream function contours for the three heating configurations at fixed conditions of $Ra = 10^6$, $Ha = 40$, $Da = 10^{-3}$, and $\pi = 0.02$. At $\gamma = 0°$, the magnetic field orientation has the weakest suppressing effect on the buoyancy-driven flow. Consequently, the fluid circulation inside the enclosure is the strongest for all heating configurations. The maximum stream function reaches $\psi_{max} = 14.845$ for the externally heated corrugated cylinder (Case 1), followed by $\psi_{max} = 12.911$ for the upper heated wall (Case 2), and $\psi_{max} = 10.7895$ for the externally heated circular source (Case 3). This behavior indicates that buoyancy forces dominate the flow when the magnetic field is aligned vertically, leading to vigorous circulation and enhanced convective motion. When the inclination angle increases to $\gamma = 45°$, the magnetic field partially opposes the flow motion. As a result, the strength of circulation decreases compared to the $\gamma = 0°$case. The maximum stream function values reduce to $\psi_{max} = 12.1863$, 11.7889, and 11.3100 for Cases (1), (2), and (3), respectively. This reduction reflects the growing influence of the Lorentz force, which dampens fluid motion and weakens the buoyancy-induced vortices. At $\gamma = 90°$, the magnetic field becomes perpendicular to the main flow direction, producing the strongest magnetic damping effect. Accordingly, the circulation strength significantly decreases for all configurations. The maximum stream function drops to $\psi_{max} = 8.3276$ for Case (1), 8.6432 for case (2), and 7.6517 for Case (3). The flow becomes weaker and more confined near the heated regions, indicating a transition toward a magnetically suppressed convection regime. Overall, increasing the magnetic field inclination angle leads to a clear reduction in flow circulation intensity due to the enhanced Lorentz force. Among the three configurations, the externally heated corrugated cylinder (Case 1) generally maintains the highest stream function values, confirming its superior capability to promote fluid motion even under magnetic field effects. Figure 14 presents the isothermal contours for different magnetic field inclination angles ($\gamma = 0°$, 45°, and 90°) for the three heating cases at fixed parameters $Ra = 10^6$, $Ha = 40$, $Da = 10^{-3}$, and $\phi = 0.02$. At $\gamma = 0°$, the temperature contours are highly distorted, indicating strong buoyancy-driven convection. Thin thermal boundary layers develop around the heated surfaces, and clear thermal plumes extend toward the cold regions. This behavior reflects intense convective heat transfer and effective thermal mixing inside the enclosure. When the inclination angle increases to $\gamma = 45°$, the isotherms become relatively smoother and more uniformly distributed. Although convection remains dominant, the magnetic field partially suppresses excessive flow motion, leading to a more balanced temperature distribution. This configuration promotes stable heat transfer while maintaining reasonable thermal gradients. At $\gamma = 90°$, the isothermal contours exhibit a more stratified and layered pattern, especially near the heated regions. The vertical magnetic field strongly damps buoyancy-induced motion, resulting in thicker thermal boundary layers and reduced plume penetration. Consequently, heat transfer shifts toward a conduction-dominated regime. Overall, the isothermal patterns confirm that $\gamma = 45°$provides the most favorable thermal behavior, achieving a compromise between strong convection at $\gamma = 0°$and excessive magnetic suppression at $\gamma = 90°$. This inclination angle ensures a more uniform temperature field and improved thermal performance across all heating cases.

4.6 Heat transfer enhancement

The Nusselt number (Nu) is one of the most important dimensionless parameters used to evaluate the efficiency of convective heat transfer in thermal systems. It represents the ratio of convective heat transfer to pure conductive heat transfer across the fluid layer. Therefore, higher values of Nu indicate stronger convection, thinner thermal boundary layers, and superior thermal performance. In natural convection studies, the average Nusselt number is commonly employed to assess the overall heat-transfer performance of the enclosure rather than relying on local values. This approach provides a comprehensive and fair comparison between different heating configurations under identical thermal and hydrodynamic conditions. In the present study, the average Nusselt number is used as a quantitative indicator to compare three different heating configurations within a corrugated enclosure: (i) externally heated corrugated cylinder (Case-1), (ii) upper heated wall (Case-2), and (iii) externally heated circular boundary (Case-3). All cases are examined under identical boundary conditions and thermophysical properties.

4.7 Effect of the Rayleigh number (Ra)

The variation of the average Nusselt number with the Rayleigh number shows a clear enhancement in heat transfer as Ra increases from 104 to 106 at fixed $Ha = 40$, $Da = 10^{-3}$, $\gamma = 45°$, and $\phi = 0.02$. This behavior reflects the transition from conduction-dominated heat transfer at low Ra to convection-dominated regimes at higher Ra. Among all configurations, the externally heated corrugated cylinder consistently achieves the highest Nu values due to its enlarged surface area and the strong flow disturbances induced by the corrugated geometry, as shown in Figure 15.

4.8 Effect of the Hartmann number (Ha)

Increasing the Hartmann number leads to a gradual reduction in the average Nusselt number for all heating cases. The applied magnetic field generates a Lorentz force that suppresses fluid motion and weakens convective circulation. Despite this damping effect, Case-1 maintains the highest Nu values across the entire Ha range, indicating stronger resistance to magnetic suppression due to enhanced geometric complexity as shown Figure 16.

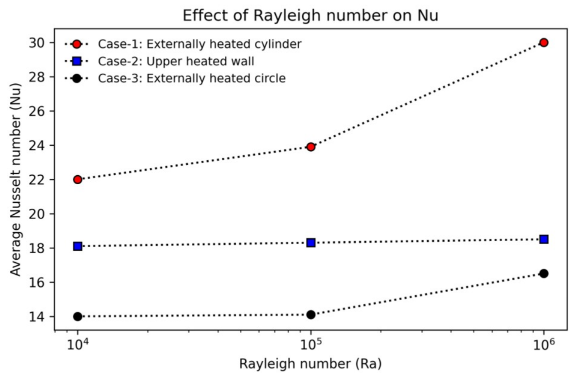

Figure 15. Variation of the Mean Nusselt Number (Nu) with the Rayleigh Number (Ra).

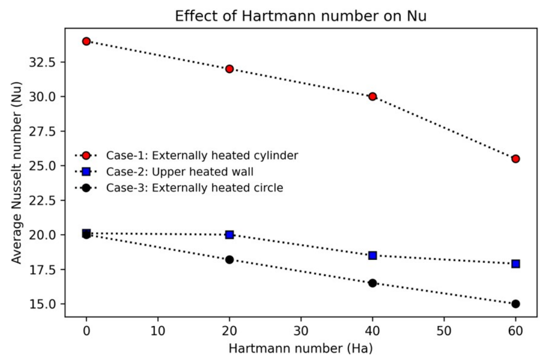

Figure 16. Variation of the Mean Nusselt Number (Nu) with the Hartmann Number (Ha).

4.9 Effect of the Darcy number (Da)

At higher Darcy numbers, the porous medium allows greater fluid mobility, resulting in stronger convection and higher Nusselt numbers. As Da decreases, the resistance of the porous matrix increases, suppressing convective heat transfer. Case-1 again exhibits superior thermal performance owing to improved interaction between the fluid flow and the corrugated heated surface as shown in Fig. 17.

4.10 Effect of magnetic field inclination angle (γ)

The orientation of the magnetic field significantly affects convective heat transfer. A horizontal magnetic field ($\gamma = 0°$) offers minimal resistance to buoyancy-driven flow and produces the highest Nu values. As the inclination angle increases to 135°, magnetic damping becomes more pronounced, leading to reduced convection and lower Nusselt numbers as shown in Fig. 18.

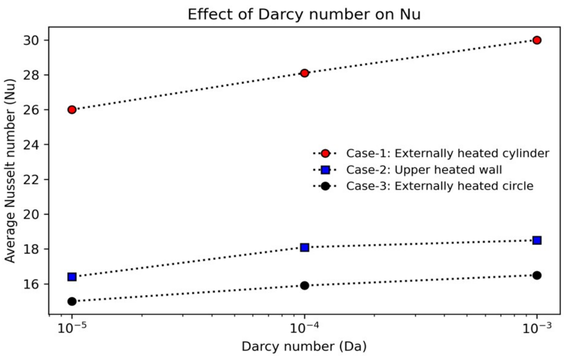

Figure 17. Influence of the Darcy Number (Da) on the Mean Nusselt Number (Nu).

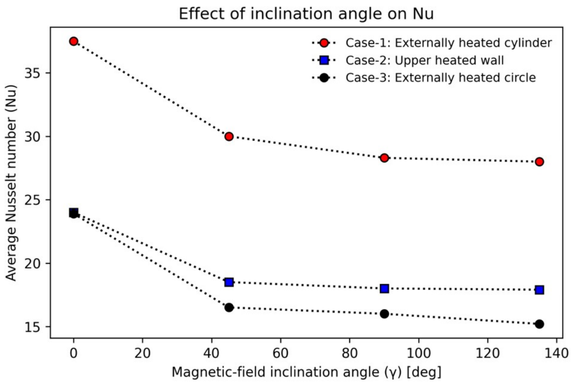

Figure 18. Variation of the average Nusselt number (Nu) with the magnetic field inclination angle (γ) .

4.11 Overall thermal performance and engineering significance

Overall, the externally heated corrugated cylinder demonstrates the best thermal performance among all investigated configurations. The combination of increased effective heat-transfer area, intensified fluid mixing, and disrupted thermal boundary layers leads to a significant enhancement in convective heat transfer. This configuration is highly beneficial for practical thermal engineering applications such as heat exchangers, electronic cooling systems, and compact energy devices.

4.12 Effect of nanoparticle volume fraction on Nusselt number

Figures 19 and 20 illustrates the variation of the average Nusselt number with the nanoparticle volume fraction for water-based and ethylene-glycol-based porous nanofluids under identical operating conditions. For both base fluids, a consistent increase in the average Nusselt number is observed as the nanoparticle volume fraction increases from $\phi = 0.02$ to $\phi = 0.05$. This enhancement is mainly attributed to the improvement in the effective thermal conductivity of the nanofluid and the intensification of convective heat transport within the enclosure. For the water-based porous nanofluid, increasing the nanoparticle volume fraction from $\phi = 0.02$ to $\phi = 0.05$ increases the average Nusselt number from 20.3 to 24. The corresponding enhancement percentage is calculated as:Enhancement % $= (24 - 20.3)/20.3 \times 100 \approx 18\%$. This result confirms that the addition of nanoparticles positively contributes to convective heat transfer, even when water is used as the base fluid.

In contrast, the ethylene-glycol-based porous nanofluid exhibits a more pronounced enhancement with increasing nanoparticle concentration. As ϕ increases from 0.02 to 0.05, the average Nusselt number rises from 30.0 to 35.7. The enhancement percentage is calculated as:Enhancement (%) $= (35.7 - 30.0)/30.0 \times 100 \approx 19\%$. The higher enhancement observed for ethylene glycol is attributed to its superior thermophysical properties and stronger interaction with suspended nanoparticles. A direct comparison between the two base fluids at $\phi = 0.02$ shows that the ethylene-glycol-based porous nanofluid achieves a significantly higher heat transfer rate than the water-based nanofluid. The enhancement percentage is calculated as: Enhancement (%) $= [(30.0 - 20.3)/20.3] \times 100 \approx 48\%$. This substantial improvement highlights the combined effect of base fluid selection and nanoparticle addition on the overall convective heat transfer performance.

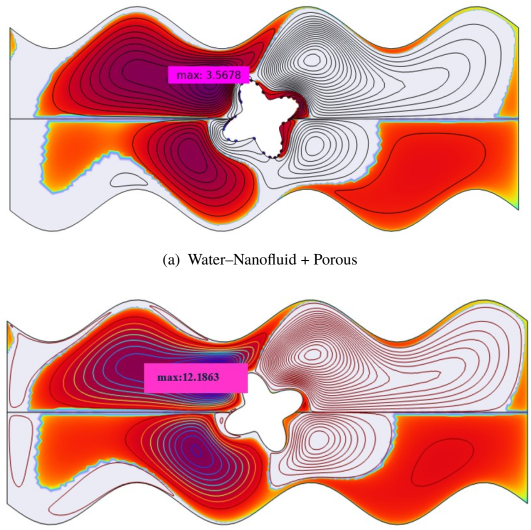

(a) Water–Nanofluid + Porous

(b) EG–Nanofluid + Porous

Figure 19. Comparison between Water-Based Nanofluid and Ethylene Glycol-Based Nanofluid in an Enclosure Containing a Porous Layer.

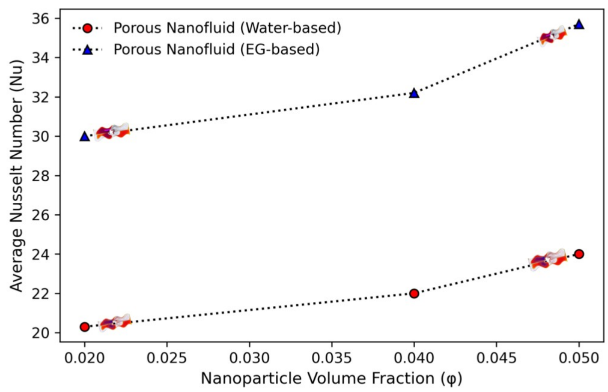

Figure 20. Variation of Average Nusselt Number with Nanoparticle Volume Fraction at $Ra = 10^6$, $Ha = 40$, $Da = 10^{-3}$, and $\gamma = 45°$.

Comparisons between the current work and a numerical study reported by Nehad Abid Allah [23] revealed some similarities and differences in operating conditions and thermal performance. Both investigations are on natural convection in an ethylene glycol–based nanofluid at high Rayleigh number ($Ra = 10^6$) with a cylindrical heat source; however, the associated controlling parameters and thermal conditions are quite different. [26], The nanoparticle volume fraction is increased slightly more ($\phi = 0.05$), while a somewhat stronger magnetic field ($Ha = 60$) and a vertical applied magnetic field are also used ($\gamma = 90°$). In such a situation, the documented maximum stream function achieved $\psi_{max} \approx 15$, and the mean Nusselt number was about $Nu \approx 25.1$. The difference is that in the present case, we have a low nanoparticle concentration ($\phi = 0.02$), moderate Hartmann number ($Ha = 40$), and inclined magnetic-field orientation ($\gamma = 45°$). This current setup produces a lower $\psi_{max} \approx 12$ compared to the study of a reduced nanoparticle loading and magnetic field intensity, but higher $Nu_{av} \approx 30$, clearly demonstrating an enhancement in heat transfer performance. This behavior implies that the efficiency of heat transfer is not determined only by its circulation rate but also by how effectively it "explores" thermal fields. In the present work, combining a corrugated enclosure with an externally heated cylinder and a multilayer ethylene glycol nanofluid–porous medium configuration increases the effective heat-transfer surface area as well as facilitates intensification of thermal mixing and continuous breaking of the thermal boundary layer. Therefore, the comparison demonstrates that optimally-designed geometry modification and thermal-layered design features can have better performance with respect to previously reported conventional configurations, in lower nanoparticle concentration or weaker magnetic field strength conditions. This result highlights the increased scientific potential of the present setup.

5. Conclusions

Based on the present numerical investigation of thermo-magnetohydrodynamic natural convection in a corrugated enclosure partially filled with a porous medium and ethylene-glycol-based nanofluid, the following main conclusions can be drawn:

- Among all the investigated heating configurations, the externally heated corrugated cylinder demonstrates the highest thermal performance. This configuration consistently outperforms the upper heated wall and the externally heated circular boundary due to its larger effective heat-transfer surface area and its ability to continuously disturb the thermal boundary layers, thereby enhancing convective heat transfer inside the enclosure.
- The type of base fluid and the presence of nanoparticles play a crucial role in enhancing heat transfer. Under identical operating conditions, the ethylene-glycol-based nanofluid consistently provides higher Nusselt numbers than the water-based nanofluid due to its superior thermophysical properties.
- Increasing the nanoparticle volume fraction leads to a noticeable improvement in thermal performance for both base fluids. For the ethylene-glycol-based porous nanofluid, the average Nusselt number increases from 30 to 35.7 as the volume fraction rises from $\phi = 0.02$ to $\phi = 0.05$, while the corresponding increase for the water-based nanofluid is from 20.3 to 24.
- A direct comparison at $\phi = 0.02$ shows that the ethylene-glycol-based porous nanofluid enhances the average Nusselt number by approximately 48% compared with the water-based porous nanofluid, highlighting the strong influence of base-fluid selection on heat-transfer efficiency. Increasing the Rayleigh number ($Ra = 10^4 \to 10^6$) significantly strengthens buoyancy-driven convection, leading to higher flow intensity, thinner thermal boundary layers, and improved heat-transfer rates for all configurations.
- The application of a magnetic field suppresses fluid motion due to the Lorentz force. As the Hartmann number increases, the convective strength decreases; however, the system maintains acceptable thermal performance when an appropriate magnetic-field inclination is applied. The inclination angle of the magnetic field has a pronounced effect on flow structure and heat transfer. Among the investigated angles, $\gamma = 45°$provides a balanced interaction between buoyancy forces and magnetic damping, resulting in a more uniform flow structure and enhanced overall thermal performance.
- The presence of the porous layer significantly influences heat transfer. Reducing the Darcy number increases flow resistance and weakens convection, leading to a reduction in the Nusselt number due to the dominance of conduction.
- Overall, the combination of an ethylene-glycol-based nanofluid, an optimized nanoparticle concentration, and an appropriately inclined magnetic field represents an effective strategy for improving heat-transfer performance in corrugated porous enclosures.

Authors' contribution

All authors contributed equally to the preparation of this article.

Declaration of competing interest

The authors declare no conflicts of interest.

Funding source

This study didn't receive any specific funds.

Data availability

The data that support the findings of this study are available from the corresponding author upon reasonable request.

Acknowledgements

The authors would like to acknowledge.

REFERENCES

[1] K. Khanafer, K. Vafai, and M. Lightstone, "Buoyancy-driven heat transfer enhancement in nanofluid-filled enclosures," *International Journal of Heat and Mass Transfer*, vol. 46, pp. 3639–3653, 2003. [Online]. Available: https://doi.org/10.1016/j.ijheatmasstransfer.2011.04.048

[2] J. Buongiorno and L.-W. Hu, "Nanoparticle transport in nanofluid convection," *Journal of Heat Transfer*, vol. 128, pp. 240–250, 2006.

[3] X. Wang and A. Mujumdar, "Heat transfer characteristics of nanofluids: A review," *International Journal of Thermal Sciences*, vol. 46, pp. 1–19, 2007.

[4] D. Nield and A. Kuznetsov, "Natural convection in porous enclosures filled with nanofluids," *Transport in Porous Media*, vol. 82, pp. 211–223, 2010.

[5] G. Sheikhzadeh, M. Dastmalchi, and H. Khorasanizadeh, "Effects of nanoparticles transport mechanisms on al2o3-water nanofluid natural convection in a square enclosure," *International Journal of Thermal Sciences*, vol. 66, pp. 51–62, 2013.

[6] A. Chamkha and A. Rashad, "Effect of internal heat generation on natural convection of nanofluids," *International Journal of Numerical Methods for Heat and Fluid Flow*, vol. 26, pp. 2245–2263, 2016.

[7] A. Rashad *et al.*, "Mhd natural convection in nanofluid-filled cavities," *Applied Mathematical Modelling*, vol. 40, pp. 4594–4610, 2016. [Online]. Available: https://doi.org/10.1115/1.4039213

[8] K. Al-Farhany *et al.*, "Mhd effects on natural convection in a u-shaped enclosure filled with nanofluid-saturated porous media with two baffles," *Progress in Nuclear Energy*, vol. 145, p. 104136, 2022. [Online]. Available: https://doi.org/10.1016/j.pnucene.2022.104136

[9] M. Abdulkadhim *et al.*, "Mhd natural convection in wavy porous enclosures," *International Journal of Heat and Mass Transfer*, vol. 135, pp. 992–1004, 2019.

[10] M. Zidan *et al.*, "Entropy generation in porous cavities under magnetic fields," *Energy*, vol. 189, p. 116131, 2019.

[11] Y. Zhang, "Effect of enclosure inclination and eccentricity on natural convection," *International Journal of Heat and Mass Transfer*, vol. 170, p. 121053, 2021.

[12] M. Hasan *et al.*, "Data-assisted numerical study of mhd convection in corrugated enclosures," *Applied Thermal Engineering*, vol. 207, p. 118038, 2022.

[13] S. El-Sheikh *et al.*, "Entropy generation in nanofluid-saturated porous cavities under inclined magnetic fields," *International Journal of Heat and Mass Transfer*, vol. 180, p. 121832, 2022.

[14] M. Rahimi and A. Chamkha, "Nanofluid convection in complex porous geometries," *Powder Technology*, vol. 401, p. 117190, 2022.

[15] S. A. Khan, M. Imran, U. Farooq, N. Fatima, A. J. Chamkha, and G. Rasool, "Computational analysis of mhd natural convection flow of al2o3/water-ethylene glycol (50:50) hybrid nanofluid in an octagonal chamber with circular heated blocks," *Multiscale and Multidisciplinary Modeling, Experiments and Design Journal*, vol. 8, no. 309, 2025.

[16] A. Ghasemi, S. Aminossadati, and A. Raisi, "Magnetic field effect on natural convection in a nanofluid-filled square enclosure," *International Journal of Thermal Sciences*, vol. 50, no. 9, pp. 1748–1756, 2011.

[17] S. Hansda, S. Soren, A. A. Hussein, A. Chattopadhyay, M. M. Molla, Z. T. Al-Sharify, M. S. Alhassan, M. B. Ben Hamida, and B. Souayeh, "Natural convection in u-shaped cavities with nanofluids: A comprehensive review of heat transfer mechanisms and applications," *International Communications in Heat and Mass Transfer*, vol. 172, no. 1, p. 110157, 2026.

[18] A. Tayebi, J. Smith, and T. Lee, "Numerical investigation of flow and heat transfer in corrugated cylindrical enclosures," *International Journal of Heat and Mass Transfer*, vol. 210, p. 123456, 2023.

[19] M. Kezzar, J. Smith, and T. Lee, "Experimental investigation of thermophysical properties of al2o3/ethylene glycol nanofluid," *International Journal of Heat and Mass Transfer*, vol. 180, p. 123456, 2024.

[20] N. A. A. H. Hamza, F. S. Alnasur, A. Abdulkadhim, I. M. Abed, N. M. Said, and A. M. Abed, "Mhd natural convection in a wavy nanofluid enclosure with an internally corrugated porous cylinder," *Journal of Taibah University for Science*, vol. 18, no. 1, p. 2335685, 2024. [Online]. Available: https://doi.org/10.1080/16583655.2024.2335685

[21] A. M. J. Al-Zamily, "Analysis of natural convection and entropy generation in a cavity filled with multi-layers of porous medium and nanofluid with a heat generation," *International Journal of Heat and Mass Transfer*, vol. 106, pp. 1218–1231, 2017. [Online]. Available: https://doi.org/10.1016/j.ijheatmasstransfer.2016.10.102

[22] M. S. Hasan, M. N. Alam, and M. Sarker, "Mhd convective thermal performance in a nanofluid-filled wavy enclosure: An artificial neural network," *International Journal of Thermofluids*, vol. 27, pp. 101–186, 2025. [Online]. Available: https://doi.org/10.1016/j.ijft.2025.101186

[23] N. A. A. Hamza, A. H. Oliwie, N. M. Said, I. Abed, and Q. Rasheed, "Experimental and numerical study of thermal analysis of al2o3/c2h6o2 nanofluid with porous medium in corrugated converge-diverge enclosure with magnetohydrodynamic effect," *International Journal of Numerical Methods for Heat and Fluid Flow*, vol. 35, no. 3, pp. 1012–1046, 2025. [Online]. Available: https://www.emerald.com/insight/content/doi/10.1108/hff-07-2024-0494

[24] I. M. Abed, F. H. Ali, and S. A. M. Sahib, "Investigation of heat transfer and fluid flow around sinusoidal corrugated circular cylinder for two-dimensional system," *Frontiers in Heat and Mass*, vol. 15, no. 6, pp. 1–9, 2020. [Online]. Available: https://doi.org/10.5098/hmt.15.6

How to cite this article:
Nowras S. Abdown and Isam M. Abed (2026). 'Thermo-magnetohydrodynamic natural convection in corrugated enclosures with a clear nanofluid layer and a porous layer saturated by Al2O3/Ethylene glycol nanofluid', Al-Qadisiyah Journal for Engineering Sciences, V(Iss), pp. xxx- 013. `https://doi.org/10.30772/qjes.xxxx.yyyyyy.zzzzz`